Negative Refraction and Partition in Acoustic Valley Materials of a Square Lattice

Zhenxiao Zhu,[1] Xueqin Huang,[1] Jiuyang Lu,[1] Mou Yan,[1] Feng Li,[1,*] Weiyin Deng,[1,†] and Zhengyou Liu[2,3,‡]

[1] *School of Physics and Optoelectronics, South China University of Technology, Guangzhou, Guangdong 510640, China*

[2] *Key Laboratory of Artificial Micro- and Nanostructures of Ministry of Education and School of Physics and Technology, Wuhan University, Wuhan 430072, China*

[3] *Institute for Advanced Studies, Wuhan University, Wuhan 430072, China*

(Received 19 May 2019; revised manuscript received 15 July 2019; published 5 August 2019; corrected 11 December 2020)

The transport behaviors of valley kink states with potential applications have become a research hotspot for acoustic waves in phononic crystals, which are usually constructed in hexagonal lattices, such as graphene and kagome lattices. We realize an acoustic valley material of a square lattice by stacking the dimerized chains of resonators in which topological phase transition is implemented by tuning the height ratio of nonequivalent resonators. The topological transports of the acoustic kink waves with reflection immunity are observed along the interface between distinct valley phases. The topological negative refraction of kink states outcoupling into free space is experimentally visualized with a tunable refraction angle. In particular, an abnormal partition transport of the acoustic kink states at the channel intersection is demonstrated in phononic crystals. These findings may have potential applications in directional vocalization, noise reduction, and beam splitting.

DOI: 10.1103/PhysRevApplied.12.024007

I. INTRODUCTION

The valley materials have attracted a great deal of attention in both condensed matter and artificial periodic materials [1–4]. The valley phases host nonzero Berry curvature distributions located near the energy extrema in momentum space, and give rise to valley bulk states in the bulk and valley kink states at the interface between topologically distinct valley phases [5,6]. The electronic valley materials were first proposed in graphene [7–10], then extended to other two-dimensional materials of hexagonal lattices [11–16], such as bilayer graphene [12–14] and transition metal dichalcogenides [15,16], and form the field of so-called valleytronics. Like the spin in spintronics, the valley may also be applied to store and carry information. The valley is usually induced by breaking the inversion symmetry of the system. The topological transports of valley kink states, such as the valley valve and beam splitting, have been observed in bilayer graphene [17–19].

Benefitting from the macroscopic scale and flexible fabrication, breaking the inversion symmetry is much easier for artificial materials and does not require an external field. Great progress has been made in the topological valley transports for electromagnetic [20–26], elastic [27–33], and acoustic [34–43] waves in artificial periodic materials. For acoustic waves, the valley bulk transports with a vortex property have been observed in phononic crystals (PCs), which may have applications in rotating the particles in an acoustic field without contact [35,36]. The valley kink transports with the reflection immunity property were observed in monolayer and bilayer hexagonal PCs [37,38], which may be used in devices with unconventional functions, such as directional acoustic antennas [39] and topological acoustic switches [40]. In addition, the valley transports studied in PCs combined the gain and loss and displayed non-Hermitian properties [41]. However, all the valley PCs mentioned above are hexagonal, and it is highly desirable to explore more intriguing transports in acoustic valley materials with other lattice types in addition to the hexagonal lattice.

In this work, we report the realization of an acoustic valley material of a square lattice in which the two nonequivalent valleys connected by time-reversal symmetry can be shifted in momentum space by tuning the structural parameters, such as the radius of the connecting tube. The valley phases are shown to possess nontrivial valley Chern numbers. The dispersions of kink states are obtained by measuring and Fourier transforming the pressure field distributions along the interface between the distinct valley phases. The topological transports of kink waves, such as the propagation along a Z shaped interface, outcoupling negative refraction, and a counterintuitive partition,

*Corresponding author. phlifeng@scut.edu.cn
†Corresponding author. dengwy@scut.edu.cn
‡Corresponding author. zyliu@whu.edu.cn

are experimentally visualized by scanning the pressure field distributions. The experiments are in agreement with the simulations, which are performed by the commercial COMSOL Multiphysics solver package.

II. RESULTS AND DISCUSSIONS

A. Valley bulk states of a square lattice PC

We construct a two-dimensional PC by arranging a square array of acoustic waveguides. Figure 1(a) shows a photo of our sample fabricated by three-dimensional (3D) printing. The unit cell contains two nonequivalent resonators A and B ($h_A \neq h_B$), which are connected by cylindrical waveguides, as shown in Figs. 1(b) and 1(c). When the height of the resonator $h_A = h_B$, there exists a pair of Dirac points located at N and N' points along the k_x axis, as the solid black lines shows in Fig. 1(d). Different from the Dirac points in graphene or kagome lattices, which are located at the high symmetry points in momentum space, the pair of Dirac points in this square lattice PC are accidental degeneracies and can be shifted at the same time by changing the structural parameters, such as radius r_1.

When $h_A \neq h_B$, as the red lines show in Fig. 1(d), the Dirac points open a bulk gap and give rise to the valley physics. Figure 1(e) shows the nontrivial Berry curvature distributions of the lower band, which mainly locate around the points N and N' with opposite magnitudes, and form two valleys connected by the time-reversal symmetry. The valley bulk states do not display the vortex configurations in the presence of twofold rotational symmetry with representations ± 1, which are different from the valley states in the hexagonal lattice, where the valley vortex configurations are induced by irreducible complex representations $e^{\pm i(2/3)\pi}$ of the threefold rotational symmetry. However, the beam splitting transport of the valley bulk states still exists, which essentially originates from the trigonal warping effect of equifrequency contours near the two valleys (see Fig. 5 in Appendix A), independent of the vortex property. Although the global Chern number in the first Brillouin zone is zero, the local valley Chern numbers C_v^N and $C_v^{N'}$, the integral of Berry curvatures near the valleys N and N', are ± 0.5. Figure 1(f) shows a phase diagram determined by the valley Chern numbers. There exist two topologically distinct valley phases where phase I is characterized by $C_v^{N,N'} = \pm 1/2$, phase II is characterized by $C_v^{N,N'} = \mp 1/2$, and the phase boundary corresponds to bulk band-gap closure.

B. Experimental observation of acoustic kink states and the reflection immunity

According to the bulk-edge correspondence, the acoustic kink states exist at the interface between phases I and II, since the difference of the valley Chern numbers of the same valley is an integer. To demonstrate the acoustic kink

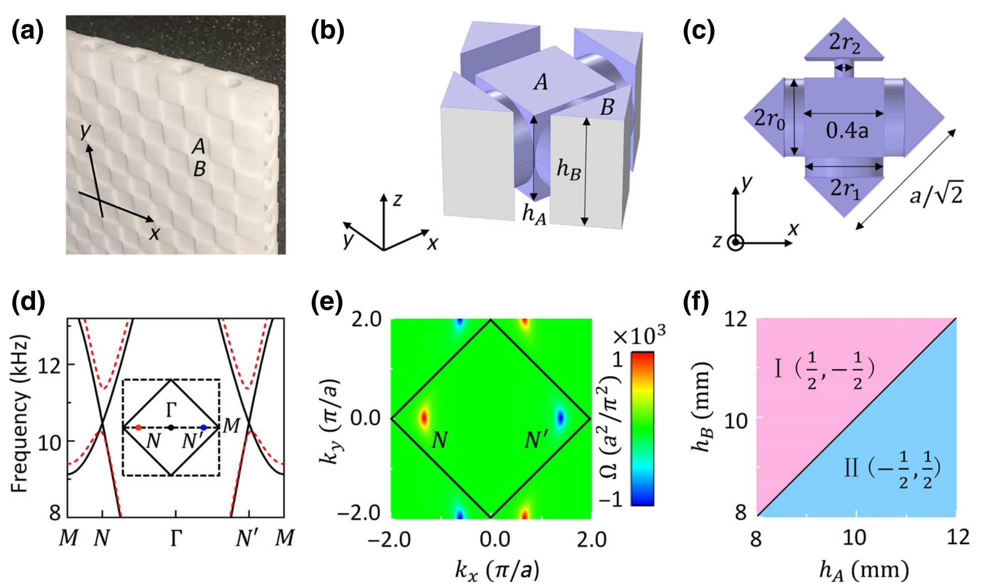

FIG. 1. Valley bulk states and topological phase diagram of a square lattice PC. (a) Photograph of a sample showing the square structure with air filling the inside. (b),(c) Side and top views of the unit cell with two nonequivalent resonators A and B. (d) The gapless and gapped bulk band structures for $h_A = 10$ mm (black lines) and 8 mm (red lines) with $h_B = 10$ mm, respectively. The black solid diamond of the insert is the first Brillouin zone. (e) Simulated Berry curvature distributions of the lower band for $h_A = 8$ mm and $h_B = 10$ mm. The Berry curvatures mainly locate near the valleys N and N'. (f) Phase diagram associated with valley Chern numbers C_v^N and $C_v^{N'}$. The black line shows the phase boundary upon closing the bulk gap when $h_A = h_B$. In all the experimental samples, the parameters of phase I are $h_A = 8$ mm and $h_B = 10$ mm, and phase II are $h_A = 10$ mm and $h_B = 8$ mm. The other structural parameters are chosen as $a = 20$ mm, $r_0 = 4$ mm, $r_1 = 4$ mm, and $r_2 = 1$ mm.

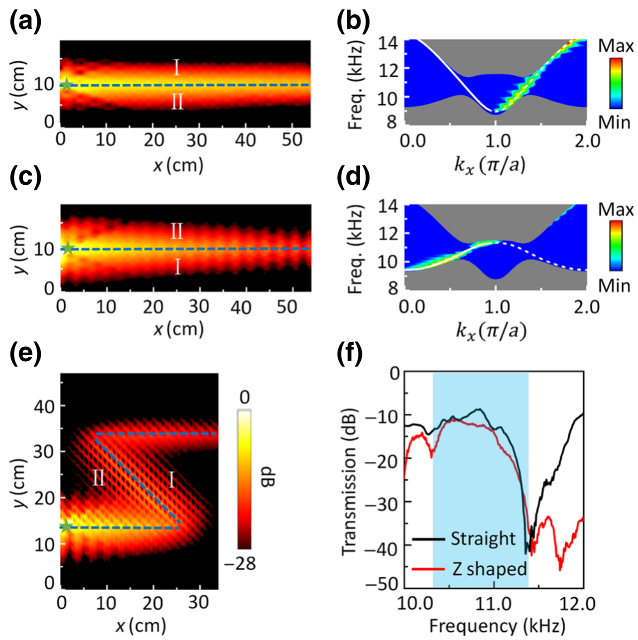

FIG. 2. Experimental observation of acoustic kink states with reflection immunity. (a) The measured pressure field distribution of the straight interface (blue dashed line) of phases I and II. (b) The corresponding measured dispersion of kink states. The solid (dashed) white line represents the simulated dispersion of kink states projected from the N (N') valley, and the gray region denotes the simulated bulk band. (c),(d) The measured pressure field distribution and dispersion of kink states are similar to (a) and (b), but with phases I and II swapped. (e) Similar to (c) but for a Z shaped interface. (f) The measured transmission spectra for the straight and Z shaped interfaces for the same length. The good coincidence in the bulk gap (blue region) indicates the robust reflection immunity of kink states. The green star denotes a point source. The field distributions are measured at $f = 10.61$ kHz.

states, we construct a straight interface separated by two PCs with distinct valley phases. In Fig. 2(a), the acoustic kink states are directly visible by the measured pressure field distributions at $f = 10.61$ kHz in the bulk gap. The projected band dispersion at this interface configuration is plotted in Fig. 2(b), where the gray region denotes the simulated bulk band. In the bulk gap, the color maps represent the experimental data, while the lines denote the simulated values. The dispersion of kink states with a positive group velocity along the x direction is evidently observed. The acoustic kink states projected from the N valley (the solid line) are not excited by a point source due to the negative group velocity, and can be excited by the source placed away from the left end of the interface. The kink states at the other interface upon swapping phases I and II are also demonstrated in Figs. 2(c) and 2(d). All the experimental and simulated dispersions of kink states are in good agreement. In addition, the damping behavior of the kink waves along the propagation direction is discussed in Appendix B. No kink states appear at the interfaces in the same phase with different structural parameters, since the difference of valley Chern numbers is zero, as shown in Fig. 7 in Appendix C.

The acoustic kink states are topologically robust against backscattering because of the intervalley decoupling and the valley-momentum locking properties, namely, the kink states projected from the N and N' valleys have opposite momentum without intervalley scattering. To verify this reflection immunity transport of the kink states, we construct a sample containing a Z shaped interface with two sharp corners (bent by 135°) between phases I and II. As shown in Fig. 2(e), the measured pressure field distributions indicate no obvious reflection appears at the two sharp corners in the propagation of waves, although the intensity of the pressure fields partly attenuates during propagation due to the air damping. In Fig. 2(f), we show the measured transmission spectra for the Z shaped interface compared with the straight interface for the same length. One can see that the two transmissions coincide well and retain high values in the entire bulk band gap (blue region), demonstrating the kink states propagate along sharply bent interfaces with a weak backscattering. What is more, the intervalley decoupling and the symmetry of the kink states can give rise to the phenomenon of valley selective excitation, as shown in Fig. 8 in Appendix D.

C. The topological negative refraction of the acoustic kink states

Next, we study the transport of acoustic kink states entering into free space through a tilted termination, and observe the topological negative refraction. As shown in Fig. 3(a), we fabricate a sample with a straight interface in which the right part of the tilted termination is the two-dimensional free space clamped by two parallel plates. The measured pressure field distributions show the kink states projected from the N valley through the tilted termination enter into the free space with the negative refraction behavior. The experimental observation agrees well with the simulation result, as shown in Fig. 3(b). The robustness of this transport comes from the reflection immunity property of kink states. To obtain the refraction angle, we show the k-space analysis on the outcoupling of the kink states, as shown in Fig. 3(c). The kink states projected from the N valley go away from the crystal and obey the conservation of momentum parallel to the crystal termination. Therefore, the refraction angle γ satisfies $\mathbf{k}_N \cdot \mathbf{e}_t = \mathbf{k}_{\text{air}} \cdot \mathbf{e}_t$, namely, $|\mathbf{k}_N| \cos 45^\circ = |\mathbf{k}_{\text{air}}| \cos(135^\circ - \gamma)$, where $\mathbf{e}_t$ is the unit vector of tilted termination, $\mathbf{k}_N$ is the wave vector of the incident kink states at N valley, and $\mathbf{k}_{\text{air}}$ is that of the refracted states at the free space and is obtained as $\gamma = 95.6^\circ$. The refraction angle in our sample can be tuned not only by changing the frequency, similar to that in hexagonal lattice system [39], but also by tuning the structural

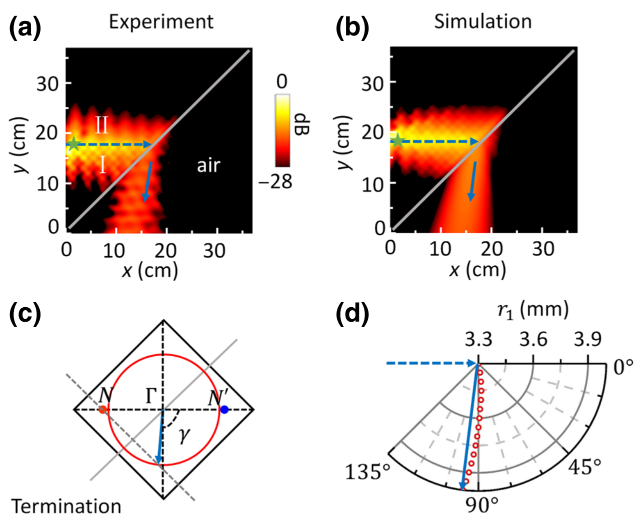

FIG. 3. The topological negative refraction of the acoustic kink states into free space. (a),(b) The experimental and simulated distributions of the pressure field at $f = 10.61$ kHz. The blue dashed line represents the interface of phases I and II, and the gray line denotes the termination. The green star is a point source and the arrows stand for the propagation directions of the kink states. (c) The k-space analysis on the outcoupling of the kink states projected from the N valley. The black solid diamond represents the first Brillouin zone and the red solid circle is the dispersion in air. (d) The simulated direction angle γ of negative refraction as a function of the radius r_1 of the connecting tube at $f = 10.61$ kHz.

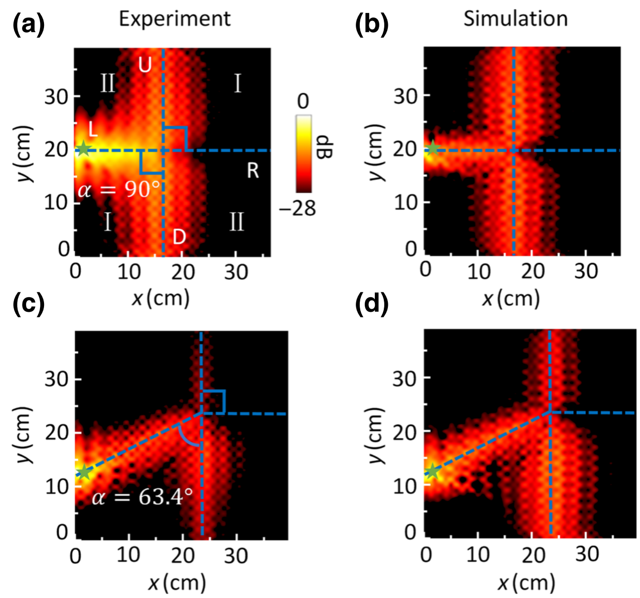

FIG. 4. Partition of acoustic kink states at the topological channel intersection. The experimental and simulated pressure field distributions in the PC with configurations featured by $\alpha = 90^\circ$ (a),(b) and $\alpha = 63.4^\circ$ (c),(d). The sample consists of two phases, I and II, with four channels labeled L (left), R (right), U (up), and D (down). The blue dashed lines denote the interfaces and the green star is a point source excited at $f = 10.61$ kHz.

parameters with shifting the positions of the valley, such as r_1, as shown in Fig. 3(d), providing an alternative way to manipulate the transport of kink states. In addition, the topological positive refraction can occur by using the kink states projected from the N' valley, as shown in Fig. 9 in Appendix E.

D. Partition of the acoustic kink states at the topological channel intersection

A fascinating current partition phenomenon at the topological channel intersection was predicted for the electronic valley kink states [6,44] and was recently experimentally verified for the elastic waves in a hexagonal lattice [32]. Interestingly, such an intriguing transport can be observed for the acoustic waves in our square lattice PC. As shown in Fig. 4(a), the system is constructed by four domains with four channels, where the top left and bottom right domains are phase II and the others are phase I. For the sample with the angle between channels D and L $\alpha = 90^\circ$, the measured pressure field distributions show that the acoustic kink waves equally enter into channels U and D from channel L and do not propagate forward into channel R. This behavior can be explained by the valley-momentum locking, namely, the kink states propagated in channels L, U, and D are projected from the N valley, but those propagated in channel R are projected from the N' valley. In addition, the symmetry of channels U and D leads to the same transmissions from L to U and D. The simulation results shown in Fig. 4(b) are consistent with the experiment.

The partition of the kink states is geometry dependent, and counterintuitively, the kink states tend to propagate along the path with a sharp turn. To demonstrate this, we construct a sample of intersection with $\alpha = 63.4^\circ$, in which channel L deviates to channel D with a sharp turn. Figures 4(c) and 4(d) show the experimental and the simulated results with good agreement. Again, the acoustic kink waves cannot propagate into channel R. Surprisingly, the propagation of the kink waves entering channel D is preponderant compared with that entering channel U. Because channel L is closer to channel D with the sharp turn near the intersection, the stronger spatial overlap of the kink states between these two channels makes the kink states couple into channel D more easily, and gives rise to the abnormal partition transport. These results provide an efficient way to manipulate acoustic kink waves.

III. CONCLUSIONS

In conclusion, we study the valley physics in a square lattice PC. Compared with the hexagonal lattice PC, our system provides a richer way to present the valley properties. The acoustic valley kink waves, propagating along the interfaces between distinct valley phases, are shown to be robust against the bending of an interface. The topological negative refraction and partition transport of the valley kink waves may apply to designing innovative acoustic devices, such as beam splitters and couplers. Moreover, it is interesting to explore the valley-dependent Landau quantization in this square lattice PC, which may induce a synthetic gauge field through the uniaxial deformation [45,46].

ACKNOWLEDGEMENTS

This work is supported by the National Natural Science Foundation of China (Grants No. 11890701, No. 11804101, No. 11572318, No. 11604102, No. 11704128, and No. 11774275); the National Key R&D Program of China (Grant No. 2018FYA0305800), the National Basic Research Program of China (Grant No. 2015CB755500); Guangdong Innovative and Entrepreneurial Research Team Program (Grant No. 2016ZT06C594); the National Postdoctoral Program for Innovative Talents (Grant No. BX201700082), China Postdoctoral Science Foundation (Grant No. 2017M622671), and the Fundamental Research Funds for the Central Universities (Grants No. 2018MS93, No. 2019JQ07, and No. 2019ZD49).

APPENDIX A: THE BEAM SPLITTING PHENOMENON OF VALLEY BULK STATES

In this section, we show the valley dependent beam splitting phenomenon. We construct a rectangular PC in phase I with $h_A = 8$ mm and $h_B = 10$ mm. Figure 5(a) shows the simulated pressure field distributions excited by a narrow Gaussian beam, which is normally incident from the bottom. One can see that the bulk states around the N and N' valley points are both stimulated because of the momentum broadening of the Gaussian beam. In the PC, the bulk states related to the N valley move toward the top left, while those related to the N' valley move toward the top right because of the different directions of the group velocities $\vec{v}_N$ and $\vec{v}_{N'}$, as shown in Fig. 5(b). This beam splitting behavior of valley bulk states essentially derives from the trigonal warping effect of equifrequency contours [the green circles in Fig. 5(b)], similar to that in the PC of a hexagonal lattice [35,36], but independent of the vortex property of the hexagonal lattice PC.

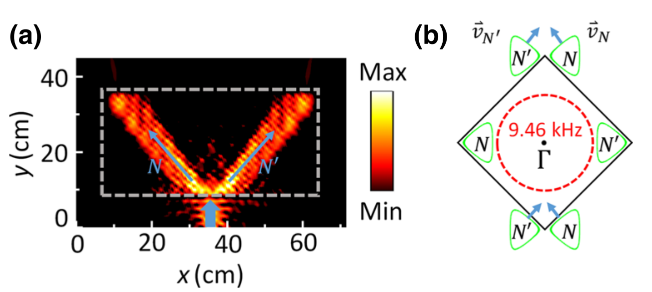

FIG. 5. Valley-dependent beam splitting transport. (a) The simulated pressure field distributions excited by a narrow Gaussian beam incident normally from the bottom of the PC at 9.46 kHz in the lower band. (b) The trigonal-like equifrequency contours at 9.46 kHz. Directions of group velocities $\vec{v}_N$ and $\vec{v}_{N'}$ around the N and N' valleys are marked by the blue arrows. The red dashed circle represents the dispersion in air at the same frequency, and the black solid diamond is the first Brillouin zone.

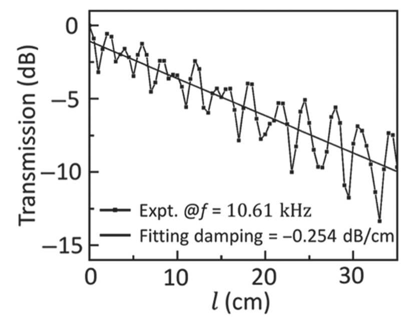

FIG. 6. The damping of the kink waves along the propagation direction for $f = 10.61$ kHz. The symbol line is the experimental data and the solid line is the fitting result.

APPENDIX B: THE DAMPING OF THE KINK WAVES ALONG THE PROPAGATION DIRECTION

In this section, we discuss the damping of the kink waves along the propagation direction. The damping of our system mainly results from the air absorption. To directly show the damping of kink waves, we perform the transmission measurement of kink waves for a straight interface sample [see in Fig. 2(c)]. As shown in Fig. 6, there is an attenuation of 10 dB when the kink waves propagate a distance of 35 cm (about 10 wavelengths) at the working frequency 10.61 kHz. That is to say, the damping coefficient is −0.254 dB/cm. Such an amount of damping is acceptable for the measurement of kink state propagation.

APPENDIX C: THE EXISTENCE OF VALLEY KINK STATES

In this section, we show the valley kink states exist at the interface between two PCs with topologically distinct valley phases, but do not exist at the interface in the same phase with different structural parameters. First, with the same structure as in the main text, the interface is composed of two PCs with distinct valley phases: one PC with $h_A = 8$ mm and $h_B = 10$ mm (phase I), and the other with $h_A = 10$ mm and $h_B = 8$ mm (phase II). As is expected, the band dispersions of the kink states exist in this configuration PC, as shown in Fig. 7(a). The red and green lines represent the band dispersions of two different interfaces connected by swapping phases I and II. The solid and dashed parts of the lines stand for the kink

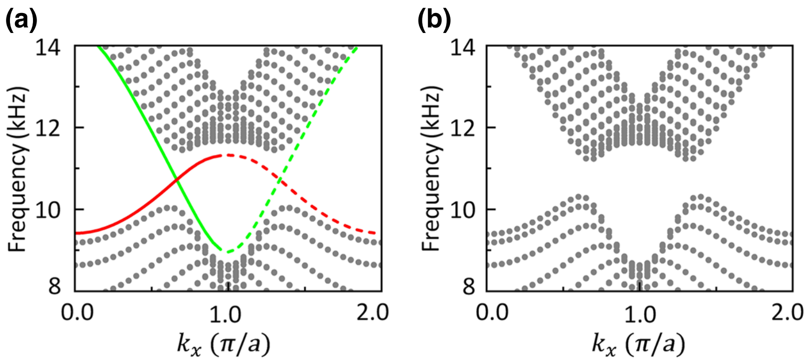

FIG. 7. The numerical validation of valley kink states. (a) Projected band dispersions for the interface separating two domains with different valley phases. Green solid and dashed lines show the kink states projected from the N and N' valleys, respectively. The red line denotes the dispersion of kink states for another interface by swapping the two valley phases. The gray solid circles represent the projected bulk band. (b) Projected band dispersions for the interface separating two domains with the same valley phase.

states projected from the N and N' valleys, respectively. Second, we construct the interface composed of two PCs with the same valley phase: one PC with $h_A = 8$ mm and $h_B = 10$ mm (phase I), and the other with $h_A = 8.5$ mm and $h_B = 10$ mm (phase II). As shown in Fig. 7(b), no kink states exist at the interfaces.

APPENDIX D: SELECTIVE EXCITATION OF ACOUSTIC KINK STATES

The selective excitation of kink states was demonstrated in a hexagonal lattice PC [37] because of the intervalley decoupling and the symmetry of the valley kink states. In this section, we show this interesting phenomenon can also exist in our square lattice PC. Figure 8(a) shows the simulated pressure field distributions of a PC with a two-interface configuration excited by a wide Gaussian beam incident from the left at $f = 10.61$ kHz in the bulk gap. One can see that the kink states at the upper channel are perfectly excited, while those at the lower channel are extremely suppressed. This selective excitation transport originates from the intervalley decoupling and the symmetry of the acoustic kink states the same as that in a hexagonal lattice PC. For the upper channel, the kink states projected from the N' valley are symmetrical within a unit cell, enabling to couple with external incident waves. However, for the lower channel, the kink states projected from the N valley are antisymmetric within a unit cell, and cannot couple with external incident waves. In Fig. 8(b), we simulate frequency dependent pressure field distributions on the exit surface of PC, presenting the channel selective phenomenon throughout the whole band gap.

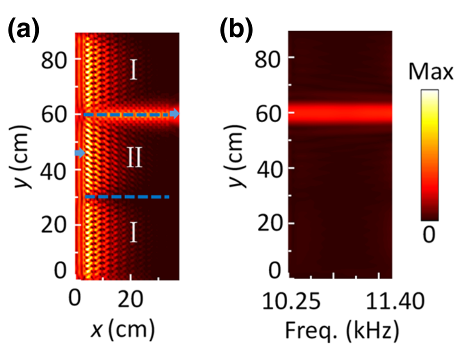

FIG. 8. Selective excitation of acoustic kink states. (a) The simulated pressure field distributions excited by a wide Gaussian beam at $f = 10.61$ kHz in the bulk gap. (b) The simulated frequency dependent pressure field distributions on the exit surface of the PC, indicating the broadband channel selection.

APPENDIX E: THE POSITIVE REFRACTION OF ACOUSTIC KINK STATES OUTCOUPLING INTO FREE SPACE

In this section, we show the topological positive refraction induced by the acoustic kink states projected from the N' valley. Similar to the refraction case in the main text, the PC system has a straight interface, but swaps phases I and II to excite the kink states projected from the N' valley, as shown in Fig. 9(a). The right part of the tilted termination is the two-dimensional free space clamped by two parallel plates. The simulated pressure field distributions at $f = 10.61$ kHz show the positive refraction behavior

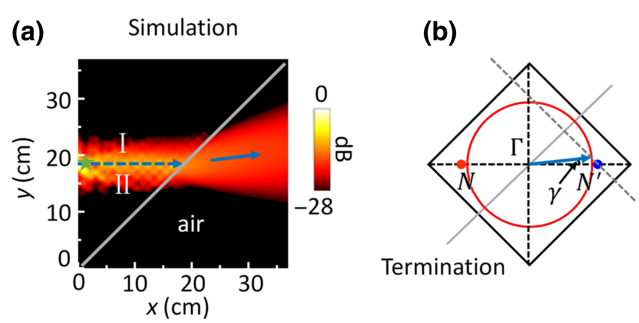

FIG. 9. The positive refraction of acoustic kink states outcoupling into free space. (a) The simulated distributions of the pressure field. The blue dashed line represents the interface of phases I and II, and the gray line denotes the termination. The green star is a point source and the arrows stand for the propagation directions of the kink states. (b) The k-space analysis on the outcoupling of the kink states projected from the N' valley. The black solid diamond represents the first Brillouin zone and the red solid circle is the dispersion in air. The excited frequency is chosen as $f = 10.61$ kHz.

when the kink states projected from the N' valley move through the tilted termination and enter into free space. From the k-space analysis on the outcoupling of the kink states, as shown in Fig. 9(b), we can find the refraction angle γ satisfies $|\mathbf{k}_{N'}|\cos 45^\circ = |\mathbf{k}_{\mathrm{air}}|\cos(45^\circ - \gamma)$, where $\mathbf{k}_{N'}$ is the wave vector of the incident kink states at N' valley and $\mathbf{k}_{\mathrm{air}}$ is that of the refracted states at the free space and is obtained as $\gamma = 5.6^\circ$.

[1] J. R. Schaibley, H. Yu, G. Clark, P. Rivera, J. S. Ross, K. L. Seyler, W. Yao, and X. Xu, Valleytronics in 2D materials, Nat. Rev. Mater. **1**, 16055 (2016).

[2] T. Ozawa, H. M. Price, A. Amo, N. Goldman, M. Hafezi, L. Lu, M. C. Rechtsman, D. Schuster, J. Simon, O. Zilberberg, and I. Carusotto, Topological photonics, Rev. Mod. Phys. **91**, 015006 (2019).

[3] X. Zhang, M. Xiao, Y. Cheng, M. H. Lu, and J. Christensen, Topological sound, Commun. Phys. **1**, 97 (2018).

[4] G. Ma, M. Xiao, and C. T. Chan, Topological phases in acoustic and mechanical systems, Nat. Rev. Phys. **1**, 281 (2019).

[5] D. Xiao, M. C. Chang, and Q. Niu, Berry phase effects on electronic properties, Rev. Mod. Phys. **82**, 1959 (2010).

[6] Y. Ren, Z. Qiao, and Q. Niu, Topological phases in two-dimensional materials a review, Rep. Prog. Phys. **79**, 066501 (2016).

[7] A. Rycerz, J. Tworzydło, and C. W. J. Beenakker, Valley filter and valley valve in graphene, Nat. Phys. **3**, 172 (2007).

[8] D. Xiao, W. Yao, and Q. Niu, Valley-Contrasting Physics in Graphene: Magnetic Moment and Topological Transport, Phys. Rev. Lett. **99**, 236809 (2007).

[9] G. W. Semenoff, V. Semenoff, and F. Zhou, Domain Walls in Gapped Graphene, Phys. Rev. Lett. **101**, 087204 (2008).

[10] R. V. Gorbachev, R. V. Gorbachev, J. C. W. Song, G. L. Yu, A. V. Kretinin, F. Withers, Y. Cao, I. V. G. A. Mishchenko, K. S. Novoselov, L. S. Levitov, and A. K. Geim, Detecting topological currents in graphene superlattices, Science **346**, 448 (2014).

[11] Z. Liu, W. Feng, H. Xin, Y. Gao, P. Liu, Y. Yao, H. Weng, and J. Zhao, Two-dimensional spin–valley-coupled Dirac, Mater. Horiz. **6**, 781 (2019).

[12] I. Martin, Y. M. Blanter, and A. F. Morpurgo, Topological Confinement in Bilayer Graphene, Phys. Rev. Lett. **100**, 036804 (2008).

[13] Z. Qiao, J. Jung, Q. Niu, and A. H. Macdonald, Electronic highways in bilayer graphene, Nano Lett. **11**, 3453 (2011).

[14] F. Zhang, A. H. MacDonald, and E. J. Mele, Valley Chern numbers and boundary modes in gapped bilayer graphene, Proc. Natl. Acad. Sci. USA **110**, 10546 (2013).

[15] X. Xu, W. Yao, D. Xiao, and T. F. Heinz, Spin and pseudospins in layered transition metal dichalcogenides, Nat. Phys. **10**, 343 (2014).

[16] K. F. Mak, K. L. McGill, J. Park, and P. L. McEuen, The valley Hall effect in MoS_2 transistors, Science **344**, 1489 (2014).

[17] L. Ju, Z. Shi, N. Nair, Y. Lv, C. Jin, J. Velasco, Jr., C. Ojeda-Aristizabal, H. A. Bechtel, M. C. Martin, A. Zettl, J. Analytis, and F. Wang, Topological valley transport at bilayer graphene, Nature **520**, 650 (2015).

[18] J. Li, K. Wang, K. J. McFaul, Z. Zern, Y. Ren, K. Watanabe, T. Taniguchi, Z. Qiao, and J. Zhu, Gate-controlled topological conducting channels in bilayer graphene, Nat. Nanotech. **11**, 1060 (2016).

[19] J. Li, R. X. Zhang, Z. Yin, J. Zhang, K. Watanabe, T. Taniguchi, C. Liu, and J. Zhu, A valley valve and electron beam splitter, Science **362**, 1149 (2018).

[20] F. Deng, Y. Sun, X. Wang, R. Xue, Y. Li, H. Jiang, Y. Shi, K. Chang, and H. Chen, Observation of valley-dependent beams in photonic graphene, Opt. Express **22**, 23605 (2014).

[21] J. W. Dong, X. D. Chen, H. Zhu, Y. Wang, and X. Zhang, Valley photonic crystals for control of spin and topology, Nat. Mater. **16**, 298 (2017).

[22] O. Bleu, D. D. Solnyshkov, and G. Malpuech, Quantum valley Hall effect and perfect valley filter based on photonic analogs of transitional metal dichalcogenides, Phys. Rev. B **95**, 235431 (2017).

[23] T. Ma and G. Shvets, All-Si valley-Hall photonic topological insulator, New J. Phys. **18**, 025012 (2016).

[24] J. Noh, S. Huang, K. P. Chen, and M. C. Rechtsman, Observation of Photonic Topological Valley Hall Edge States, Phys. Rev. Lett. **120**, 063902 (2018).

[25] F. Gao, H. Xue, Z. Yang, K. Lai, Y. Yu, X. Lin, Y. Chong, G. Shvets, and B. Zhang, Topologically protected refraction of robust kink states in valley photonic crystals, Nat. Phys. **14**, 140–144 (2017).

[26] X. D. Chen, F. L. Zhao, M. Chen, and J. W. Dong, Valley-contrasting physics in all-dielectric photonic crystals: Orbital angular momentum and topological propagation, Phys. Rev. B **96**, 020202 (2017).

[27] J. Vila, R. K. Pal, and M. Ruzzene, Observation of topological valley modes in an elastic hexagonal lattice, Phys. Rev. B **96**, 134307 (2017).

[28] J. J. Chen, S. Y. Huo, Z. G. Geng, H. B. Huang, and X. F. Zhu, Topological valley transport of plate-mode waves in a homogenous thin plate with periodic stubbed surface, AIP Adv. **7**, 115215 (2017).

[29] S. Y. Huo, J. J. Chen, H. B. Huang, and G. L. Huang, Simultaneous multi-band valley-protected topological edge states of shear vertical wave in two-dimensional phononic crystals with veins, Sci. Rep. **7**, 10335 (2017).

[30] T. W. Liu and F. Semperlotti, Tunable acoustic valley–hall edge states in reconfigurable phononic elastic waveguides, Phys. Rev. Appl. **9**, 014001 (2018).

[31] R. K. Pal and M. Ruzzene, Edge waves in plates with resonators: an elastic analogue of the quantum valley Hall effect, New J. Phys. **19**, 025001 (2017).

[32] M. Yan, J. Lu, F. Li, W. Deng, X. Huang, J. Ma, and Z. Liu, On-chip valley topological materials for elastic wave manipulation, Nat. Mater. **17**, 993 (2018).

[33] N. Lera, D. Torrent, P. San-Jose, J. Christensen, and J. V. Alvarez, Valley Hall phases in kagome lattices, Phys. Rev. B **99**, 134102 (2019).

[34] B. Xie, H. Liu, H. Cheng, Z. Liu, S. Chen, and J. Tian, Acoustic topological transport and refraction in a Kekulé lattice, Phys. Rev. Appl. **9**, 014001 (2019).

[35] J. Lu, C. Qiu, M. Ke, and Z. Liu, Valley Vortex States in Sonic Crystals, Phys. Rev. Lett. **116**, 093901 (2016).
[36] L. Ye, C. Qiu, J. Lu, X. Wen, Y. Shen, M. Ke, F. Zhang, and Z. Liu, Observation of acoustic valley vortex states and valley-chirality locked beam splitting, Phys. Rev. B **95**, 174106 (2017).
[37] J. Lu, C. Qiu, L. Ye, X. Fan, M. Ke, F. Zhang, and Z. Liu, Observation of topological valley transport of sound in sonic crystals, Nat. Phys. **13**, 369 (2016).
[38] J. Lu, C. Qiu, W. Deng, X. Huang, F. Li, F. Zhang, S. Chen, and Z. Liu, Valley Topological Phases in Bilayer Sonic Crystals, Phys. Rev. Lett. **120**, 116802 (2018).
[39] Z. Zhang, Y. Tian, Y. Wang, S. Gao, Y. Cheng, X. Liu, and J. Christensen, Directional acoustic antennas based on valley-hall topological insulators, Adv. Mater. **30**, 1803229 (2018).
[40] Z. Zhang, Y. Tian, Y. Cheng, Q. Wei, X. Liu, and J. Christensen, Topological acoustic delay line, Phys. Rev. Appl. **9**, 034032 (2018).
[41] M. D. Wang, L. P. Ye, J. Christensen, and Z. Y. Liu, Valley Physics in Non-Hermitian Artificial Acoustic Boron Nitride, Phys. Rev. Lett. **120**, 246601 (2018).
[42] X. Ni, M. A. Gorlach, A. Alu, and A. B. Khanikaev, Topological edge states in acoustic Kagome lattic, New J. Phys. **19**, 055002 (2017).
[43] B. Xia, S. Zheng, T. Liu, J. Jiao, N. Chen, H. Dai, D. Yu, and J. Liu, Observation of valleylike edge states of sound at a momentum away from the high-symmetry points, Phys. Rev. B **97**, 155124 (2018).
[44] Z. Qiao, J. Jung, C. Lin, Y. Ren, A. H. MacDonald, and Q. Niu, Current Partition at Topological Channel Intersections, Phys. Rev. Lett. **112**, 206601 (2014).
[45] X. Wen, C. Qiu, Y. Qi, L. Ye, M. Ke, F. Zhang, and Z. Liu, Axial-field-induced chiral channels in an acoustic Weyl system, Nat. Phys. **15**, 352 (2019).
[46] V. Peri, M. Serra-Garcia, R. Ilan, and S. D. Huber, Acoustic Landau quantization and quantum Hall like edge states, Nat. Phys. **15**, 357 (2019).

Correction: Byline footnote labels for “Corresponding author” for three authors were inadvertently deleted during the production cycle and have now been inserted.